

## PAPER • OPEN ACCESS

# Label-free detection of live cancer cells and DNA hybridization using 3D multilayered plasmonic biosensor

To cite this article: Shuyan Zhu *et al* 2018 *Nanotechnology* **29** 365503

View the [article online](#) for updates and enhancements.

## You may also like

- [On-chip label-free plasmonic based imaging microscopy for microfluidics](#)  
P Arora and A Krishnan
- [Nonlinear optics in plasmonic nanostructures](#)  
N C Panoiu, W E I Sha, D Y Lei et al.
- [Three-dimensional multilayer concentric bipolar electrodes restrict spatial activation in optic nerve stimulation](#)  
Eleonora Borda, Vivien Gaillet, Marta Jole Ildelfonsa Airaghi Leccardi et al.

# Label-free detection of live cancer cells and DNA hybridization using 3D multilayered plasmonic biosensor

Shuyan Zhu<sup>1,2</sup> , Hualin Li<sup>2,3</sup>, Mengsu Yang<sup>2,3</sup> and Stella W Pang<sup>1,2</sup> 

<sup>1</sup> Department of Electronic Engineering, City University of Hong Kong, Kowloon, Hong Kong

<sup>2</sup> Centre for Biosystems, Neuroscience, and Nanotechnology, City University of Hong Kong, Kowloon, Hong Kong

<sup>3</sup> Department of Biomedical Sciences, City University of Hong Kong, Kowloon, Hong Kong

E-mail: [pang@cityu.edu.hk](mailto:pang@cityu.edu.hk)

Received 12 April 2018, revised 22 May 2018

Accepted for publication 31 May 2018

Published 4 July 2018



## Abstract

Three-dimensional (3D) multilayered plasmonic nanostructures consisting of Au nanosquares on top of SU-8 nanopillars, Au asymmetrical nanostructures in the middle, and Au asymmetrical nanoholes at the bottom were fabricated through reversal nanoimprint technology. Compared with two-dimensional and quasi-3D plasmonic nanostructures, the 3D multilayered plasmonic nanostructures showed higher electromagnetic field intensity, longer plasmon decay length and larger plasmon sensing area, which are desirable for highly sensitive localized surface plasmonic resonance biosensors. The sensitivity and resonance peak wavelength of the 3D multilayered plasmonic nanostructures could be adjusted by varying the offset between the top and bottom SU-8 nanopillars from 31% to 56%, and the highest sensitivity of 382 and 442 nm/refractive index unit were observed for resonance peaks at 581 and 805 nm, respectively. Live lung cancer A549 cells with a low concentration of  $5 \times 10^3$  cells  $\text{ml}^{-1}$  and a low sample volume of  $2 \mu\text{l}$  could be detected by the 3D multilayered plasmonic nanostructures integrated in a microfluidic system. The 3D plasmonic biosensors also had the advantages of detecting DNA hybridization by capturing the complementary target DNA in the low concentration range of  $10^{-14}$ – $10^{-7}$  M, and providing a large peak shift of 82 nm for capturing  $10^{-7}$  M complementary target DNA without additional signal amplification.

**Keywords:** plasmonic nanostructures, three-dimensional, asymmetrical three metal layers, reversal nanoimprint lithography, live cancer cell detection

(Some figures may appear in colour only in the online journal)

## 1. Introduction

Quantitative and rapid detection of live cancer cells and DNA hybridization are critical aspects of cancer diagnosis, gene mutation, food safety, and environment protection. Traditional methods for disease detection such as cell viability

array [1], polymerase chain reaction [2], and enzyme-linked immunosorbent array [3] entail fluorescent labeling require long preparation time, steps, and highly trained technicians. Magnetic particles coated with synthesized nanostructured gold (Au) were used to detect DNA hybridization by surface enhanced Raman spectroscopy. However, large sample volume of  $100 \mu\text{l}$  was required to detect DNA hybridization and the detection sensitivity was limited to  $2.5 \times 10^{-7}$  M [4]. Because of these requirements, they are not suitable for point of care (POC) devices, which should be inexpensive, portable, label-free, require small sample volume, and are



Original content from this work may be used under the terms of the [Creative Commons Attribution 3.0 licence](https://creativecommons.org/licenses/by/3.0/). Any further distribution of this work must maintain attribution to the author(s) and the title of the work, journal citation and DOI.

capable of rapid diagnosis in real-time measurements with high sensitivity. The development of POC devices is a promising solution for home care system with improved patient survival and health delivery efficiency. Integration of micro-fluidic technology with various detection methods such as optical [5, 6], electrochemical [7], and mechanical [8] transduction have been employed for miniaturized POC devices. Among these detection methods, localized surface plasmon resonance (LSPR)-based optical biosensors have shown significant advantages of being fast, highly sensitive, simple, and providing high signal-to-noise ratio [9].

LSPR occurs when the collective oscillation of free electrons in noble metal nanoparticles (NPs) is resonant with the incident light frequency, resulting in strongly confined surface plasmons (SPs) on the surface of NPs. The extremely intense localized SPs are highly sensitive to analyte binding interactions, such as small molecules, ligand-receptor binding, DNA hybridization, and DNA-protein interactions on the NP surface because these bindings change the permittivity of the dielectric around the surface and the resonance frequency of the localized SPs by increasing the dielectric screening and reducing the restoring force for collective electronic oscillations [10]. Colloidal Au nanorods at 0.5 nM could detect 0.01 IU ml<sup>-1</sup> hepatitis B surface antigen with a peak redshift of 6 nm [11]. 500 nm diameter Au NPs could detect 120  $\mu$ l retinal pigment epithelium cells at a concentration range of 10<sup>4</sup>–10<sup>6</sup> cell ml<sup>-1</sup> [12].

Au colloidal solution and Au NPs on glass are the most commonly used LSPR biosensors [13]. The Au colloidal solution is easy to synthesize, but its sensitivity is low and not applicable for device miniaturization [14]. In contrast, chip-based Au NP is easier to be integrated with other components and is a promising candidate for use as a miniaturized POC device [15]. The LSPR spectra of chip-based Au NPs depend on its material, size, geometry, distribution, and effective refractive index (RI) in the surrounding area [16]. Most researchers focus on changing the two-dimensional (2D) NP shapes such as dots, holes, rings, and asymmetric split-ring. For these 2D plasmonic nanostructures, their plasmon modes only originate from the coupling between adjacent structures in the *x*-*y* plane, thus limiting their plasmon modes and sensitivities. Quasi three-dimensional (3D) plasmonic nanostructures could provide multiple plasmonic modes and improve the sensitivity from the hybrid coupling effect of two different plasmonic layers, that is, Au nanostructures on the top and bottom. However, the most sensitive plasmon mode of quasi-3D plasmonic nanostructures occurs at wavelengths above 1000 nm, which falls into the light absorbance range of water and is unsuitable for live cell detection. Bloch wave SP polariton creates the plasmon mode at lower wavelength with a maximum sensitivity of up to 100 nm/refractive index unit (RIU), therefore limiting their application for cell detection at low concentration [17, 18]. 3D self-assembly of multilayered Au nanorods show higher electromagnetic (EM) field intensity and sensitivity than single layer Au nanorods and could detect malachite green at a concentration down to 1  $\times$  10<sup>-10</sup> M. However, the uniformity and reproducibility of self-assembly multilayered Au nanorods were low and

difficult to control [19]. Au-titanium dioxide-Au plasmonic nanocup array was demonstrated to detect carcinoembryonic antigen with detection limit down to 10 ng ml<sup>-1</sup>. This sensing mechanism was based on changes of transmission intensity, which is not as reliable for accurate analysis compared to detecting resonance peak shifts [20]. To address these issues and detect live cells with high sensitivity, 3D multilayered plasmonic nanostructures were proposed, which consist of Au nanosquares on top of SU-8 nanopillars, Au asymmetrical nanostructures in the middle, and Au asymmetrical nanoholes at the bottom to generate multiple plasmon modes with high sensitivity in the visible and near-infrared regions. To the best of our knowledge, our study is the first to report the 3D multilayered plasmonic nanostructures with Au layers on the top, middle, and bottom and the application on detecting live cancer cells and DNA hybridization with high sensitivity.

The 3D multilayered plasmonic nanostructures were fabricated by reversal nanoimprint lithography (RNIL) with simultaneous thermal and ultraviolet (UV) (STU) exposure. In contrast to a typical nanoimprint process, UV exposure was first applied to crosslink the top SU-8 resist and released from the stamp to stack on the bottom SU-8 nanopillars to achieve two layers of nanopillars. RNIL is a high throughput and low-cost technology for fabricating 3D structures with high uniformity over large area and is more suitable for producing biosensors with 3D structures compared to other techniques such as focused ion beam, electron beam lithography, or atomic force microscopy. Typically, to fabricate 3D nanostructures over 1 cm<sup>2</sup>, focus ion beam or electron beam lithography will take many days to complete the direct write patterning. However, reversal nanoimprint technology allows the same patterning to be finished in just a few minutes. The cost of the equipment for nanoimprint is usually more than 10 times lower than systems for focus ion beam or electron beam lithography. The 3D multilayered plasmonic nanostructures integrated with polydimethylsiloxane (PDMS) microfluidic channels could be used to detect live lung cancer A549 cells at a concentration of 5  $\times$  10<sup>3</sup> cell ml<sup>-1</sup> and sample volume of 2  $\mu$ l with a peak redshift of 4 nm. The 3D multilayered plasmonic nanostructures were also useful for detecting DNA hybridization with high sensitivity because of their large plasmonic sensor area and multiple resonance modes that resulted from hybrid plasmonic coupling of top Au nanosquares, middle Au asymmetrical nanostructures, and bottom Au asymmetrical nanoholes.

Recently, the detection limit for DNA hybridization on Au nanodisks with 120 nm diameter has been reported to be 10<sup>-9</sup> M with a peak shift of 0.18 nm [21]. Higher detection sensitivity with larger peak shift of 3.1 nm have been demonstrated on Au nanorings as a result of EM field enhancement in both the inside and outside of the ring structures from the dipolar resonance mode [22]. Anisotropic NPs with sharp tips and large aspect ratio can further improve the sensitivity by concentrating the localized SPs on the sharp tips, resulting in a peak shift of 35 nm for 10<sup>-6</sup> M of the complementary DNA target [23]. Additionally, several methods amplify the sensitivity by using complementary DNA as a linker for binding of proteins and particles after

hybridization. For instance, DNA label with Au nanorods and nanostars could improve the detection limit to  $2 \times 10^{-10}$  M DNA hybridization with a peak shift of 0.35 nm [24]. The combination of DNA-linked avidin-tagged glucose oxide and silver (Ag) particle etching process could detect the complementary DNA target as low as  $10^{-14}$  M with a peak shift of 2.5 nm [25]. However, this amplification method needs an extra binding process and immersion in acid for Ag particle etching, making the detection process more complicated and time consuming. Ag particles show higher sensitivity than Au particles due to its low imaginary dielectric constant, but they may not suitable to be used as plasmonic biosensors because of the oxidation and degradation [26]. In our study, the 3D multilayered plasmonic biosensor detected DNA hybridization without binding extra particles for signal amplification, and the detection range for DNA hybridization was  $10^{-14}$ – $10^{-7}$  M of the complementary DNA target. A large peak shift of 82 nm occurred from capturing  $10^{-7}$  M of the complementary DNA target. Therefore, the 3D multilayered plasmonic nanostructures fabricated by RNIL are high performance biosensors for detecting live cancer cells at low concentrations with large peak shift and DNA hybridization with high sensitivity.

## 2. Experiment and methods

### 2.1. Fabrication process of 3D multilayered plasmonic nanostructures

Figure 1 shows the fabrication process of the 3D multilayered plasmonic nanostructures by stacking SU-8 nanopillars with offset. Intermediate polymer stamp (IPS) with 280 nm wide, 535 nm pitch, and 500 nm deep nanoholes was used for RNIL. Fabrication details of the IPS soft stamp and SU-8 nanopillars on glass were described in our previous paper [18]. As shown in figure 1, IPS was first treated with trichloro-(1H, 1H, 2H, 2H-perfluorooctyl) silane (PFOTS) (Sigma-Aldrich, 97%) for 20 min at 80 °C, followed by spin-coating SU-8 photoresist without crosslinking. Before the RNIL was conducted, the SU-8 nanopillar-imprinted glass was treated with an O<sub>2</sub> plasma to increase the SU-8 surface energy from 25.1 to 70.3 mN m<sup>-1</sup>, as shown in figure 1. The surface energy of IPS with PFOTS treatment was 23.7 mN m<sup>-1</sup>, which was much lower than 70.3 mN m<sup>-1</sup> for nanopillars on glass to make sure that top SU-8 nanopillars could successfully transfer from IPS onto the bottom SU-8 nanopillars. The surface energy was measured by contact angle measurements with Owens calculation (DropMeter<sup>TM</sup> Standard A-100, Ningbo, China). In contrast to typical STU process, UV exposure for 10 s at 45 °C and 5 bar was first applied to crosslink the top SU-8, followed by imprinting at 80 °C and 40 bar for 120 s. After RNIL, the IPS stamp was demolded at 20 °C, and the 3D multilayered nanostructures with residual layer were formed and hard-baked at 150 °C for 10 min to achieve good adhesion and mechanical properties of the layers of SU-8 nanopillars. 3D multilayered nanostructures could be generated by removing the residual SU-8

layer using O<sub>2</sub>/SF<sub>6</sub> reactive ion etching (RIE) with 20/2 sccm flow rates, 20 mTorr pressure, and 100 W rf power. Finally, 2 nm chromium (Cr) and 30 nm Au films were thermally evaporated on the 3D multilayered nanostructures to form three different plasmonic layers, which consisted of top Au nanosquares, middle Au asymmetrical nanostructures, and bottom Au asymmetrical nanoholes.

### 2.2. Measurement of refractive index sensitivity (RIS)

Optical measurements were done in a UV–visible spectrophotometer (UV-1700, Shimadzu, Japan). A normal incident light source under a wavelength range of 450–1100 nm was used to illuminate the 3D multilayered plasmonic nanostructures. The RIS of the 3D plasmonic sensors were measured by immersing the plasmonic nanostructures in certified RI liquids (Cargille Laboratories, NJ, USA) with RI of 1.305, 1.404, and 1.504.

### 2.3. Fabrication process of microfluidic chip

The microfluidic channel, having dimensions of 80 mm long, 60 mm wide, inlet and outlet diameter of 2 mm, and 30 μm high, was fabricated in PDMS. A silicon (Si) stamp was first fabricated by photolithography and etched by deep RIE. The Si stamp was then treated by PFOTS to form an anti-stiction layer. Liquid PDMS (Dow Corning Sylgard 184) was casted on the Si stamp and cured on a hot plate at 80 °C for 6 h. The PDMS microfluidic platform was then peeled off from the Si stamp, and the inlet and outlet holes were punched with a 0.5 mm biopsy punch. The surface of PDMS microfluidic platform and glass containing the 3D multilayered plasmonic nanostructures were treated with an O<sub>2</sub> plasma at 250 mTorr, 5 sccm, 80 W, and 30 s. Then the PDMS microfluidic platform was aligned and bonded on the glass substrate containing the 3D multilayered plasmonic nanostructures. After bonding, sterile phosphate buffered saline solution was immediately injected into the microfluidic device to maintain hydrophilicity of the PDMS microfluidic channel.

### 2.4. Cell culture and immobilization

An O<sub>2</sub> plasma was used to treat the surface of the 3D multilayered plasmonic biosensors to make them hydrophilic and cell-adhesive [27]. This allowed A549 live cancer cell to adhere on the surface of the plasmonic nanostructures and be detected by the optical measurements without antibody binding. The 3D structures also promoted cell adhesion due to their increased surface area [28]. Microfluidic chip was first sterilized under UV treatment for 30 min, and the channel was washed thrice with Dulbecco's modified eagle's medium (DMEM) with 10% fetal bovine serum (Invitrogen, CA, USA). Live lung cancer A549 cells were added to calcein AM (Life technology) at concentration of 4 μg ml<sup>-1</sup> for 30 min for fluorescence labeling and washed thrice with DMEM. A549 cells at different concentration in 2 μl of DMEM were loaded into the microfluidic channels, and live cell concentration was detected optically using a Nikon eclipse Ni-E upright fluorescence microscopy. The A549 cells was immobilized on the

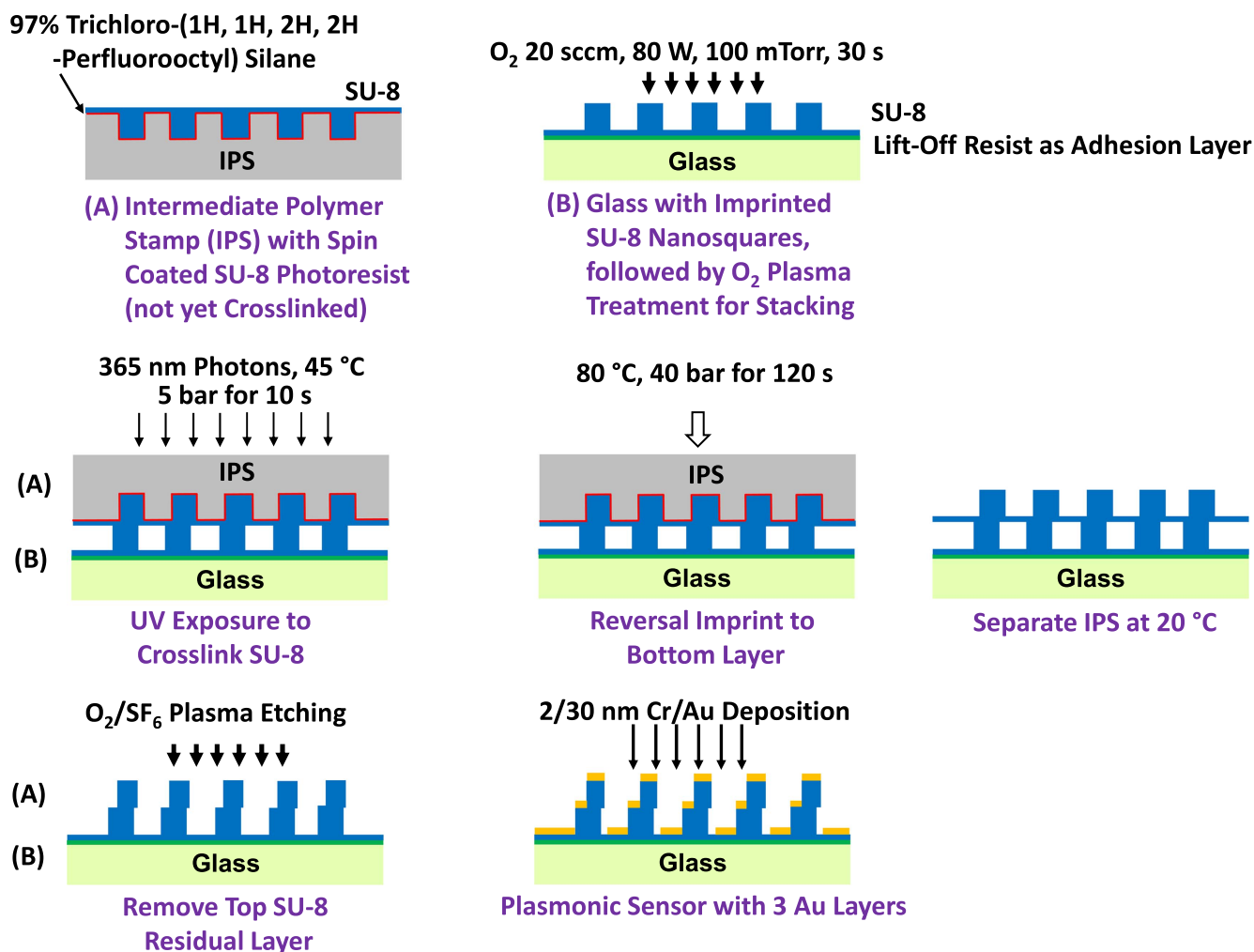


**Figure 1.** Fabrication process of 3D multilayered plasmonic nanostructures by reversal imprint with offset.

hydrophilic surface of the 3D nanostructures at 37 °C with 5% carbon dioxide for 4 h.

## 2.5. Immobilization of DNA probe and hybridization with complementary DNA target

The 3D multilayered plasmonic nanostructures were washed thrice with MilliQ water and air dried at room temperature. After washing and air-drying,  $10^{-6}$  M thiol-modified DNA probe (5'-ACT CAT CAC CCT CCA AAC AAC AAT AAT CCT-SH-3') in H<sub>2</sub>O (30  $\mu$ l) was added to the surface of the 3D structures at room temperature for 30 min. The thiol group would react with Au atoms at room temperature and bind to the surface covalently to form a self-assembled monolayer [29]. H<sub>2</sub>O and 1% bovine serum albumin were used to wash the device. 10  $\mu$ l of complementary DNA target (5'-AGG ATT ATT GTT GTT TGG AGG GTG ATG AGT AGT ATG TGG AGG TTA GGT GGA-3') or non-complementary DNA (5'-CAA AAA CAA AAA CAA AAA CAA AAA-3') were injected into the device, followed by 1 h incubation at 37 °C for hybridization, washing with 1 ml MilliQ water, and air-drying. No concentration enrichment was used for DNA hybridization detection. The molecular weight of the thiol-modified DNA probe, complementary DNA target and non-complementary

DNA were 9188, 7359, and 16 101.5 g mol<sup>-1</sup> respectively. DNA oligonucleotides were purchased from Shanghai Sangon Biological Engineering Technology and Service Co., Ltd (Shanghai, China) and purified using high performance liquid chromatography.

## 2.6. Imaging using scanning electron microscopy

The 3D multilayered plasmonic nanostructures were observed under a scanning electron microscope (SEM) (XL30 ESEM-FEG, Philips Electronics, Netherlands), after thermal evaporation of 2/30 nm Cr/Au films. ImageJ software (NIH, MD, USA) was used to compute the offset between the top and bottom SU-8 nanopillars of the 3D multilayered plasmonic nanostructures.

## 2.7. Numerical calculations by finite difference time domain (FDTD) method

The FDTD method based on Lumerical FDTD solutions (Vancouver, Canada) was employed to investigate the normalized extinction spectra and EM field distribution of 2D, quasi-3D, and 3D multilayered plasmonic nanostructures. The simulation region was 9  $\mu$ m<sup>2</sup> in the *x*-*y* plane, and a plane



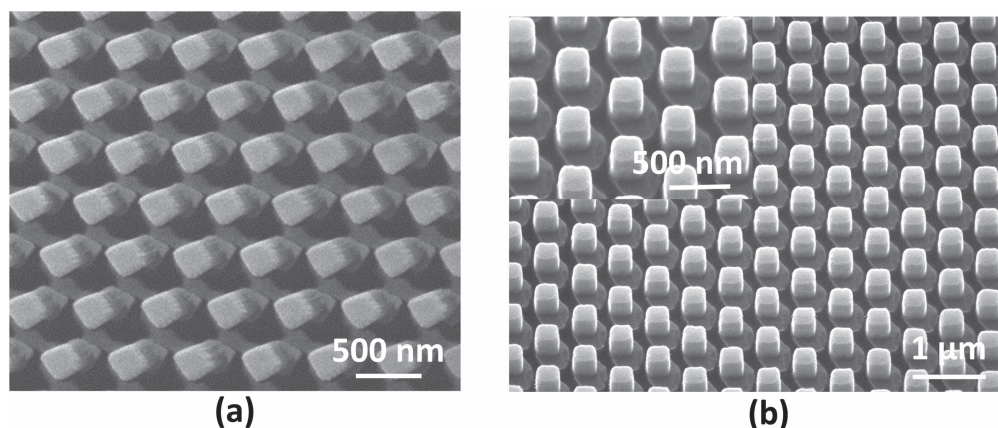


**Figure 2.** Micrographs of 3D multilayered nanostructures. (a) 32% offset and (b) 50% offset.

wave with wavelength of 400–1200 nm and polarization along horizontal direction was used as the normal incident light. Periodic boundary conditions were adopted in both the  $x$ - and  $y$ -directions, and a perfect match layer was applied in both the top and bottom along the  $z$ -direction to minimize the reflection errors. A frequency domain power monitor was placed behind the simulated structure to monitor the transmission spectra. The simulations were performed in 3D and a mesh size of 5 nm was used in most of the region except a smaller mesh size of 2 nm was used around the plasmonic nanostructures. The size and distribution of the 3D multilayered plasmonic nanostructures were obtained from the SEM measurements. The dielectric constant of Au was obtained from CRC handbook and SU-8 polymer was assumed to 1.61 [30].

### 3. Results and discussion

#### 3.1. Reversal nanoimprint to uniformly stack multilayered nanostructures

Reversal nanoimprint technology was developed to produce uniform and reproducible 3D multilayered nanostructures by stacking of nanopillars. As shown in figure 1, UV exposure for 10 s at 45 °C and 5 bar was applied to first crosslink the top SU-8 resist and prevent it from flowing into the bottom layer of SU-8 nanopillars. After crosslinking the top SU-8 layer, the imprint temperature and pressure were increased to provide uniform transfer of the top layer nanopillars to the bottom layer. No transfer occurred at lower temperature and pressure of 65 °C and 10 bar because the top SU-8 layer was already crosslinked. Therefore, a higher pressure of 40 bar was necessary to increase the transfer yield. Under 40 bar, most of the top SU-8 nanopillars still stayed on the IPS stamp after unmolding due to poor adhesion between the top and bottom SU-8 nanopillars. Treating the polymer at higher temperature increased the adhesion between polymers [31], so a higher temperature of 80 °C was applied to enhance the adhesion between top and bottom SU-8 nanopillars, thus improving the transfer yield to 80% at 80 °C and 40 bar. The residual layer was etched using 20/2 sccm O<sub>2</sub>/SF<sub>6</sub>, 20 mTorr,

and 100 W. Figure 2 shows the micrographs of 3D multilayered plasmonic nanostructures. As shown in figure 2(a), the offset between the top and bottom SU-8 nanopillars was 32%, and the top SU-8 nanopillars were 200 nm wide with 535 nm pitch and 400 nm deep, while the bottom SU-8 nanopillars were 280 nm wide with 535 nm pitch and 500 nm deep. The offset generated the area of Au asymmetrical nanostructures as the middle Au layer. Figure 2(b) shows the 3D multilayered plasmonic nanostructures with 50% offset. As shown in figure 2(b), the top SU-8 nanopillars were stacked uniformly on the bottom SU-8 nanopillars with good adhesion after baking at 150 °C.

#### 3.2. Simulation of 2D, quasi-3D, and 3D multilayered plasmonic nanostructures

Figure 3 shows the micrographs and simulated EM field intensity distributions for 2D plasmonic nanosquares, quasi-3D plasmonic nanostructures with Au on the top and bottom of the nanopillars and 3D multilayered plasmonic nanostructures with Au on the top, middle, and bottom of the stacked nanopillars. The incident light polarization and resonance wavelength for each FDTD plot were shown in figure 3 and in the figure caption. As shown in figure 3(a), EM field intensity was enhanced around the 2D nanosquares and the EM field coupling occurred between adjacent nanosquares. Quasi-3D plasmonic nanostructures consisting of Au nanosquares on top and Au nanoholes on bottom increased the EM field intensity by the hybrid LSPR and Fabry–Perot mode between the two Au layers, as shown in figure 3(b) [18]. On the other hand, asymmetrical nanostructures generated Fano resonance and enhanced EM field, resulting in higher intensity than symmetrical nanostructures [32]. As shown in figures 3(c), 3D multilayered plasmonic nanostructures consisted of three different plasmonic layers, namely, top layer Au nanosquares, middle layer Au asymmetrical nanostructures, and bottom layer Au asymmetrical nanoholes, resulted in hybrid plasmonic coupling of these three plasmonic layers with enhanced EM field around the Au layers on the top, middle, and bottom. The EM field intensity around the Au structures formed ‘hot-spots’, which were sensitive to the changes of the effective RI of the surrounding

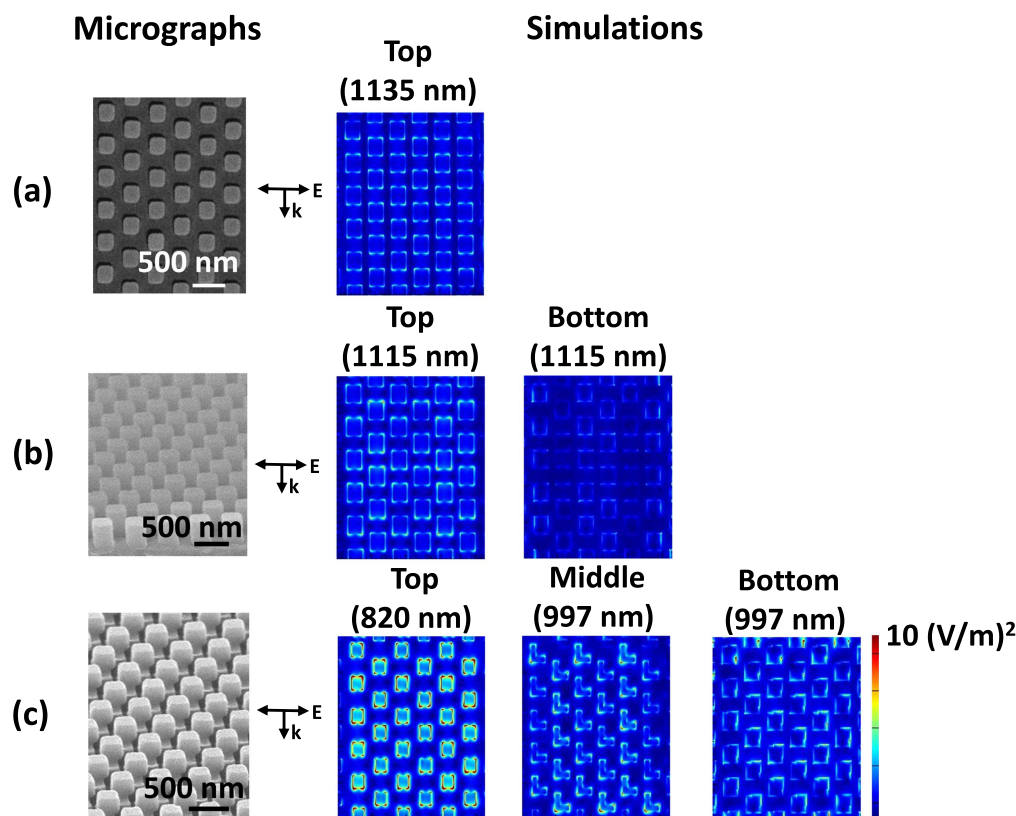


**Figure 3.** Micrographs and simulated EM field distributions for (a) 2D plasmonic Au nanosquares (1135 nm), (b) quasi-3D plasmonic nanostructures with Au on top (1115 nm) and bottom (1115 nm), and (c) 3D multilayered plasmonic nanostructures with Au on top (820 nm), middle (997 nm), and bottom (997 nm).

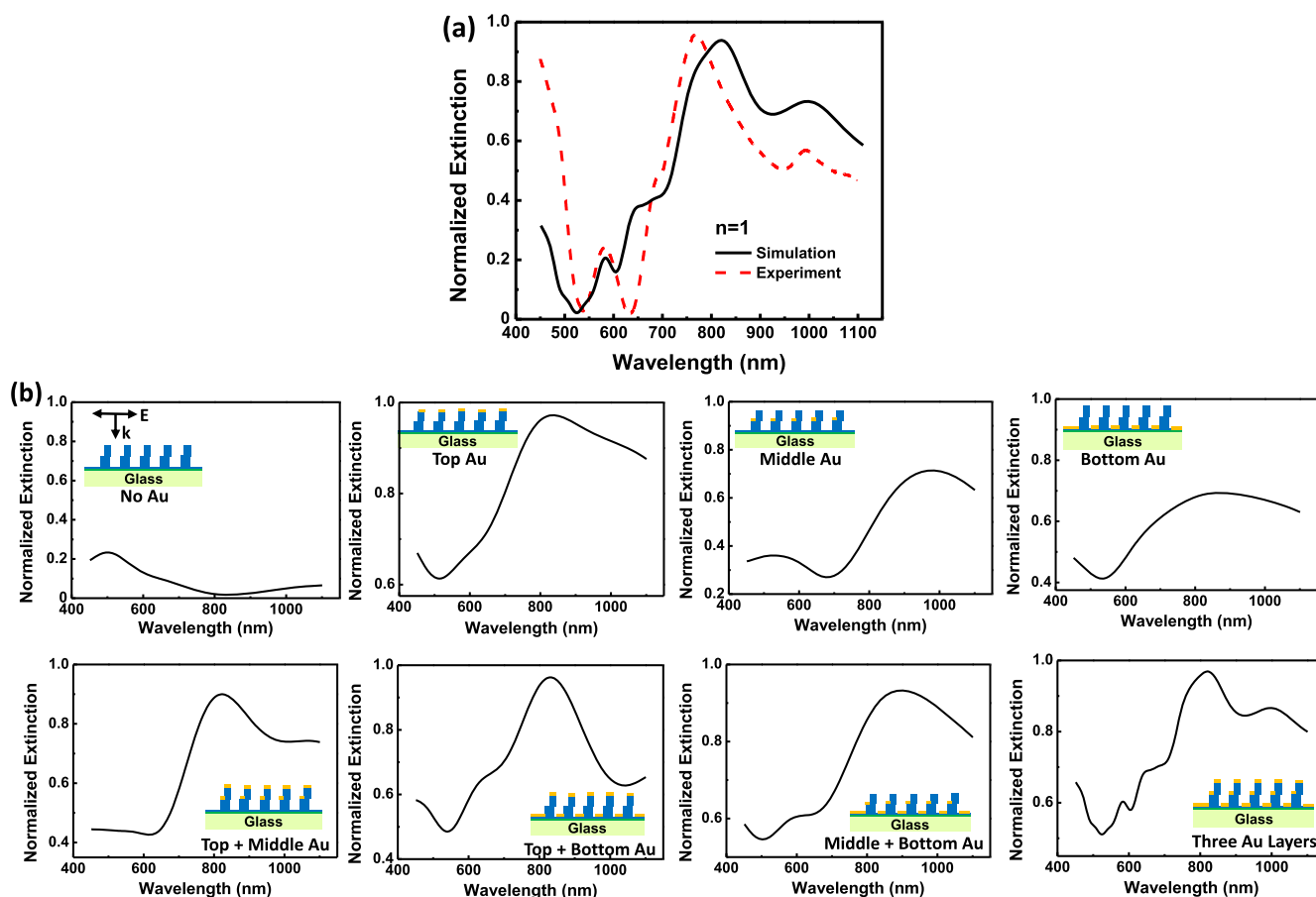
microenvironment, while the 3D structures provided large plasmon sensing area. The EM field intensity and plasmon sensing area of 3D multilayered plasmonic nanostructures was higher and larger than 2D and quasi-3D plasmonic nanostructures, which could be used as LSPR biosensor with higher sensitivity than 2D and quasi-3D plasmonic nanostructures.

Figure 4(a) shows the simulated (black) and measured (red) extinction spectra for 3D multilayered plasmonic nanostructures with 50% offset. Three main resonance peaks at 583 (P1), 820 (P2), and 997 (P3) nm were observed in the simulated spectra, which matched well with the experimental results. To understand the hybrid plasmonic coupling of the top layer of Au nanosquares, middle layer of Au asymmetrical nanostructures, and bottom layer of Au asymmetrical nanoholes, 3D multilayered plasmonic nanostructures with different combinations of the top, middle, and bottom Au layers on stacked SU-8 nanopillars were simulated by the FDTD method. As shown in figure 4(b), a weak resonance peak at 500 nm was present in the 3D structures without any Au layer because of light diffraction [33]. The 3D structures with top Au nanosquares and bottom Au asymmetrical nanoholes showed resonance peaks at 833 and 866 nm, respectively. Two resonance peaks at 539 and 976 nm were observable in the 3D structures with middle layer of Au asymmetrical nanostructures. Then, 3D structures with two different plasmonic layers were simulated to further investigate the hybrid plasmonic coupling effects and their influence

in the three resonance peaks. For 3D structures with top and bottom Au layers, the resonance peak around 583 nm was absent, indicating that the resonance peak at 583 (P1) nm was due to the middle Au asymmetrical nanostructures. The hybrid plasmonic coupling of Au layers on top, middle, and bottom was responsible for the resonance peak at 820 (P2) nm because the 3D structures with top and middle or top and bottom Au layers showed a resonance peak around 820 nm. For 3D structures with middle and bottom Au layers, two resonance peaks at 600 and 910 nm appeared. In comparison with 3D structures containing the top Au layer, the 3D structures with middle and bottom Au layers resulted in redshifting the resonance peak to 910 nm, indicating that the resonance peak at 997 (P3) nm mainly arose from the hybrid plasmon coupling of Au layers in the middle and bottom. Therefore, the middle Au asymmetrical nanostructures generated the resonance peak at 583 (P1) nm, and the resonance peak at 820 (P2) nm came from the hybrid plasmonic coupling of Au layers on the top, middle, and bottom. The hybrid plasmonic coupling of middle layer Au asymmetrical nanostructures and bottom Au asymmetrical nanoholes was responsible for the resonance peak at 997 (P3) nm.

### 3.3. RIS as function of offset between top and bottom SU-8 nanopillars

Figure 5 shows the measured extinction spectra for 3D multilayered plasmonic nanostructures with (a) 31%, (c) 49%,



**Figure 4.** (a) Simulated (black) and measured (red) extinction spectra for 3D multilayered plasmonic nanostructures with 50% offset. (b) Simulated extinction spectra for 3D multilayered plasmonic nanostructures with different combinations of top, middle, and bottom Au layers on stacked SU-8 nanopillars.

and (e) 56% offset. Insets in (a), (c), and (e) show the micrographs of the corresponding structures. The sensitivity and resonance peak wavelength of the 3D multilayered plasmonic nanostructures could be tailored by varying the offset between the top and bottom SU-8 nanopillars. Certified RI liquids with different RI were used to measure their extinction spectra and sensitivities. As shown in figures 5(a), 3D multilayered plasmonic nanostructures with 31% offset showed three resonance peaks at 576, 820, and 1086 nm in liquid with RI of 1.305, and all resonance peaks were redshifted in liquid with increasing RI from 1.305 to 1.504. The measured sensitivities of the resonance peaks at 576 and 820 nm were 296 and 346 nm/RIU, respectively. The resonance peak at 1086 nm redshifted out of the detection range. With the nanopillar offset increasing from 31% to 49%, larger plasmonic area was obtained in middle Au asymmetrical nanostructures, and higher sensitivities of 346 and 397 nm/RIU were obtained for resonance peaks at 587 and 820 nm, respectively, as shown in figure 5(c). Figure 5(e) shows the normalized extinction spectra of 3D multilayered plasmonic nanostructures with 56% offset. The measured sensitivity for resonance peaks at 581 and 805 nm were 382 and 442 nm/RIU, respectively. The figure of merit (FOM) for the 581 nm peak was as high as 9.5. In comparison with 3D multilayered plasmonic nanostructures that had 31% and 49% offsets, an

offset of 56% generated higher sensitivities of 382 and 442 nm/RIU due to the larger plasmonic sensing area of the middle Au asymmetrical nanostructures, as shown in figure 5(g). Figures 5(b), (d), and (f) shows that the resonance peaks of the 3D multilayered plasmonic nanostructures with different offsets redshifted linearly when the RI of the surrounding medium was increased. As the resonance peaks shifted linearly with increasing RI from 1.305 to 1.504, it is expected that the detection sensitivity based on resonance peak shift will hold for small changes in analyte concentration. Previous studies showed that metal–dielectric–metal multilayer structures [34] and quasi-3D plasmonic nanostructures [18] could also generate multiple resonance modes in the 450–1100 nm region from plasmonic hybrid coupling of LSPR with SP polaritons and Fabry–Perot cavity mode, respectively. However, their maximum sensitivities were only up to 179 and 167 nm/RIU with low FOM less than 2, which may not be suitable for live cell detection at low concentration. An iso-Y shaped nanopillar was also engineered to detect biomolecules in visible and near-infrared region with sensitivity of 256 nm/RIU and FOM of 1.98 [35]. In contrast, the present 3D multilayered plasmonic nanostructures could improve the FOM to 9.5 and increased the sensitivity up to 442 nm/RIU compared to previously reported structures,



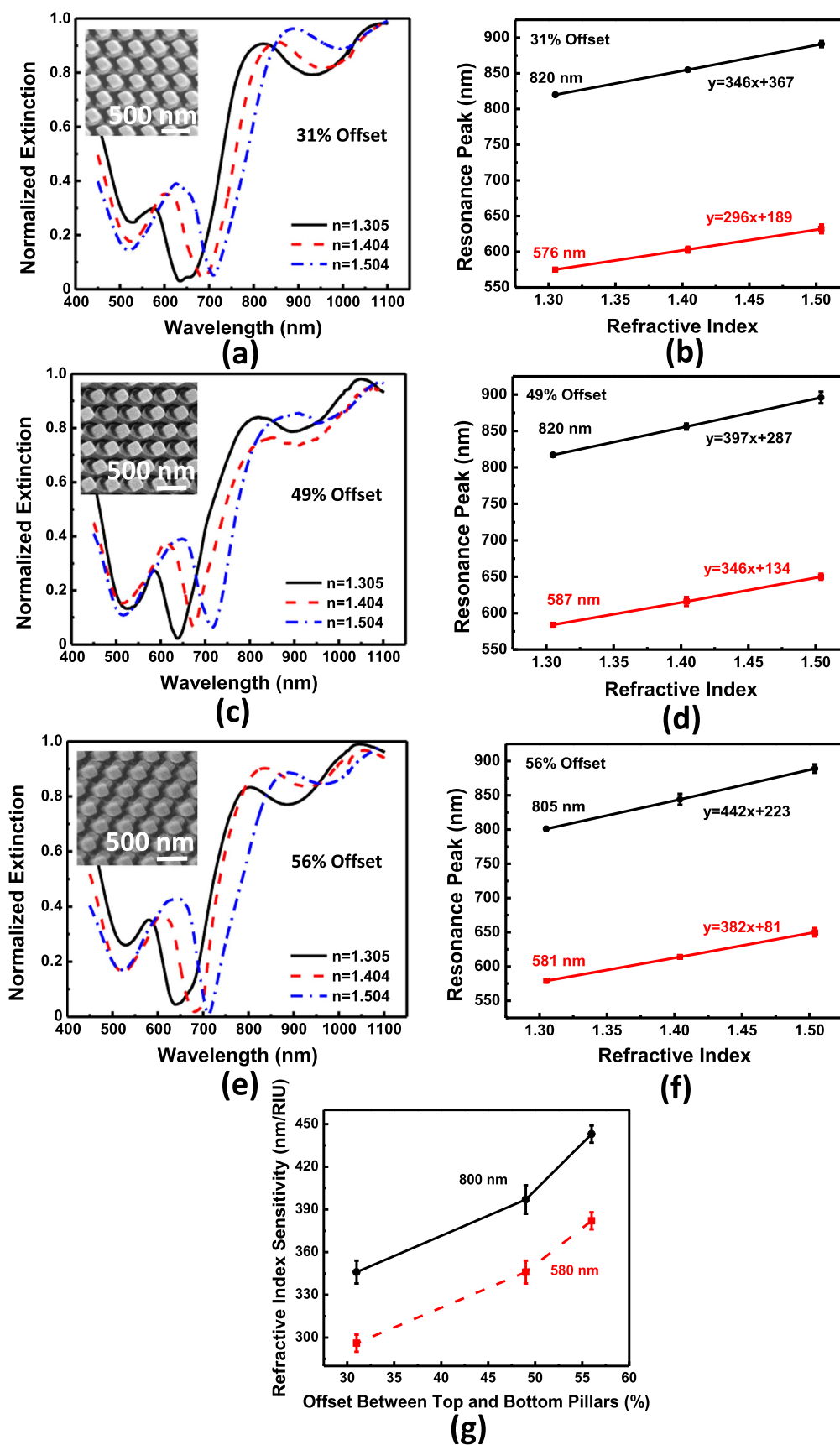


**Figure 5.** Measured extinction spectra for 3D multilayered plasmonic nanostructures with (a) 31%, (c) 49%, and (e) 56% offset. (b), (d), and (f) Linear relationship between LSPR peak wavelength and refractive index of surrounding medium for corresponding offset. (g) RIS as function of offset between top and bottom SU-8 nanopillars.

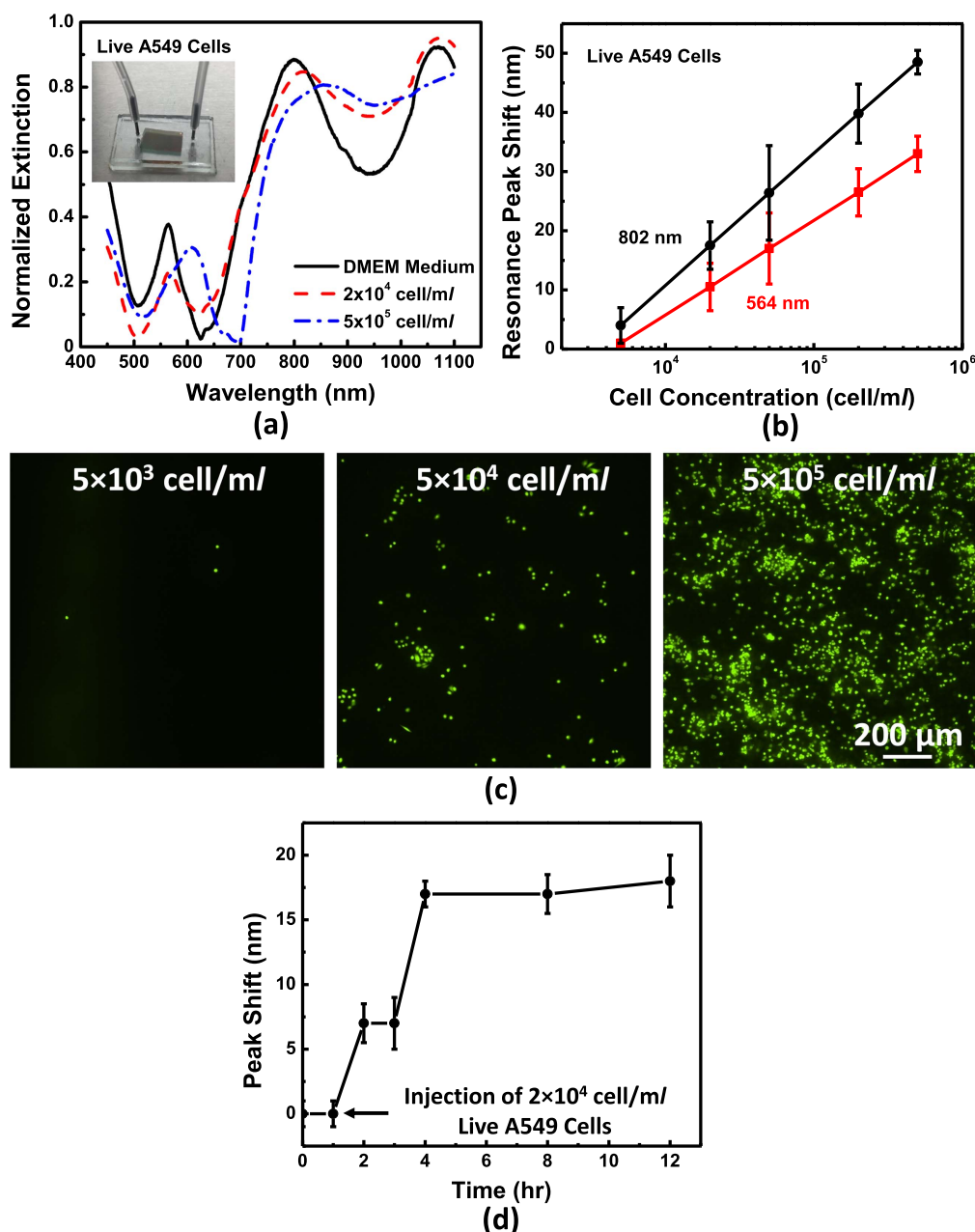


**Figure 6.** (a) Normalized extinction spectra of 3D multilayered plasmonic nanostructures with 56% offset in DMEM medium and with live lung cancer A549 cells of  $2 \times 10^4$  and  $5 \times 10^5$  cell  $\text{ml}^{-1}$ . (b) Resonance peak shifts as function of A549 cell concentration. (c) Fluorescent micrographs of live lung cancer A549 cells on 3D multilayered plasmonic nanostructures at concentrations of  $5 \times 10^3$ ,  $5 \times 10^4$ , and  $5 \times 10^5$  cell  $\text{ml}^{-1}$ . (d) Peak shift as a function of immobilization time for  $2 \times 10^4$  cell  $\text{ml}^{-1}$  live A549 cells.

making them useful for live cell detection in the visible and near-infrared region.

### 3.4. Live cell detection of A549 lung cancer cells

Figure 6 shows the detection of live lung cancer A549 cell at different concentrations. As shown in the inset of figure 6(a), a microfluidic channel with the 3D multilayered plasmonic nanostructures allowed live cell detection under a small sample volume of  $2 \mu\text{l}$ . Three resonance peaks at 564, 802,

and 1069 nm were observed for this microfluidic device in DMEM medium. All resonance peaks redshifted after live A549 cells at different concentrations were injected into the microfluidic channel and attached on the surface of the 3D multilayered plasmonic nanostructures. The intact morphology of A549 cells on 3D nanostructures was influenced by the size and spacing of SU-8 nanopillars. In this work, the diameter and spacing of the top SU-8 nanopillars were 200 and 335 nm, respectively. Although the A549 cell size was much larger than the nanopillars and their spacing, the

extensions of microvilli with typical size of 100 nm and filopodia with diameter less than 300 nm from the A549 cells could fill in between the SU-8 nanopillars and resulted in the resonance peak shifts. For live A549 cells at high concentration of  $5 \times 10^5$  cell  $\text{ml}^{-1}$ , resonance peaks at 564 and 802 nm were redshifted by 36 and 52 nm to 600 and 854 nm, respectively. There was no concentration enrichment for live A549 cell detection as the cells and DMEM medium were confined in the microfluidic platform with the plasmonic sensors. Unlike the detection of dry cancer cells in air, the integration of microfluidic channel with 3D multilayered plasmonic nanostructures could monitor the growth of cancer cells in a suitable culture environment, which was helpful for investigating the response of cancer cells to culture environment and therapy. The detection of live cancer cells was difficult than dry cancer cells because the RI difference between DMEM medium and live cancer cells was much lower than air and dry cancer cells [36]. Figure 6(b) shows that the detection range for live A549 cells was  $5 \times 10^3$ – $5 \times 10^5$  cell  $\text{ml}^{-1}$ . The large peak shift of 3D multilayered nanostructures at live A549 cells of  $5 \times 10^3$ – $5 \times 10^5$  cell  $\text{ml}^{-1}$  was useful for cancer therapy study, because the interaction of cancer cells and natural killer cells in confinement region could be dynamic monitored without using complex, expensive and time consuming confocal microscopy [37]. The fluorescent micrographs of live lung cancer A549 cells on 3D multilayered plasmonic nanostructures were shown in figure 6(c). Figure 6(d) shows the peak shift as a function of immobilization time for live A549 cells with a concentration of  $2 \times 10^4$  cell  $\text{ml}^{-1}$ . As shown in figure 6(d), the live A549 cells started to adhere on the surface of the 3D multilayered plasmonic nanostructures after 2 h and the peak shift was stable after 4 h. In comparison, colloidal Au NPs could only detect cell concentrations above  $7.5 \times 10^5$  cell  $\text{ml}^{-1}$  and it required a large sample volume of 200  $\mu\text{l}$  [38]. Au nanoislands with nickel doped graphene was used previously to detect 3-nitrotyrosine biomarkers with a detection limit of 0.13  $\text{pg ml}^{-1}$  in phosphate buffered silane solution [39]. However, the uniformity, size, and morphology of these Au nanoislands were difficult to control and the detection sensitivity was limited to 100 nm/RIU [40]. Au nanoparticle based LSPR biosensor integrated with microfluidics showed sensitivity of 120 nm/RIU and detected liver cancer antibody at a concentration of 25  $\text{ng ml}^{-1}$  [41]. 50  $\mu\text{l}$  anti-human IgG with concentration of 1.5  $\mu\text{g ml}^{-1}$  could be detected by 3D Au nanocups with a peak shift of 16.8 nm and sensitivity of 195 nm/RIU [42]. The 3D multilayered plasmonic nanostructures with 56% offset between the nanopillars showed higher sensitivity up to 442 nm/RIU, could detect low concentration live cancer cells down to  $5 \times 10^3$  cell  $\text{ml}^{-1}$  using a small sample volume of 2  $\mu\text{l}$ . Therefore, this 3D multilayered LSPR biosensor could be used as a high performance detector for low concentration live cell monitoring.

### 3.5. Resonance peak shift as function of complementary DNA target concentration

The resonance peak shift was related to the changes in the effective RI of the surrounding microenvironment of the 3D

multilayered plasmonic nanostructures, which could be described as:

$$\nabla \lambda_{\text{res}} = S \Delta n (1 - e^{-t/l_d}), \quad (1)$$

where  $S$  is the RIS,  $\Delta n$  is the RI difference between the adsorbate and the surrounding medium,  $t$  is the effective adsorbate thickness, and  $l_d$  is plasmon decay length. Due to the evanescent character of the localized surface plasmon modes, the effective sensitivity and sensing depth were limited to the range of plasmon decay length. The RIS was influenced by the size, shape, and material of the 3D plasmonic nanostructures [43]. The effective adsorbate thickness was calculated based on the plasmon decay length. The sensitivity of 3D plasmonic sensors in response to RI changes induced by adsorbate layer will decrease exponentially if the thickness of the layer is larger than the plasmon decay length [44]. To increase sensitivity, it is desirable to have larger effective adsorbate thickness for larger peak shift. For 2D plasmonic nanostructures, their  $l_d$  was typically tens of nanometers and it became  $\sim 100$  nm for quasi-3D plasmonic nanostructures due to the hybrid coupling of the LSPR and Fabry–Perot cavity modes [33]. For 3D plasmonic nanostructures, the introduction of asymmetrical plasmonic layers could result in dark mode resonance with longer  $l_d$  and higher FOM, which are useful for biomolecule detection with high sensitivity [45].

In comparison with cell detection where the typical cell size is 10–20  $\mu\text{m}$ , DNA hybridization could be more easily detected by the 3D multilayered plasmonic nanostructures since DNA molecules are smaller in size and they could occupy most of the sensing area in three plasmonic layers. Figure 7(a) shows the schematic for DNA hybridization detection as the 3D multilayered plasmonic nanostructures were first bound with the thiol-modified probe DNA. The complementary target DNA could specifically hybridize with the probe DNA and resulted in a resonance peak shift because of the increased effective RI on 3D multilayered plasmonic nanostructures due to DNA hybridization. The non-complementary DNA could not hybridize with the probe DNA and will not affect the resonance peak. Figure 7(b) shows the normalized extinction spectra of the 3D multilayered plasmonic nanostructures with 56% offset and with probe and complementary target DNA of  $10^{-10}$  and  $10^{-7}$  M. All resonance peaks were redshifted after capturing the complementary target DNA. Figure 7(c) shows the peak shifts as function of complementary target DNA concentration. The international union of pure and applied chemistry method was used to calculate the limit of detection with the numerical factor set to three [46]. As shown in figure 7(c), the resonance peaks were redshifted linearly for target DNA concentration between  $10^{-13}$  and  $10^{-8}$  M and the detection limit was calculated to be  $7 \times 10^{-14}$  M. For larger concentration of complementary target DNA, the peak shift increased and a large peak shift of 82 nm was obtained with  $10^{-7}$  M of the complementary target DNA. Therefore, the 3D multilayered plasmonic biosensor could be used to detect the complementary target DNA with a large concentration range of

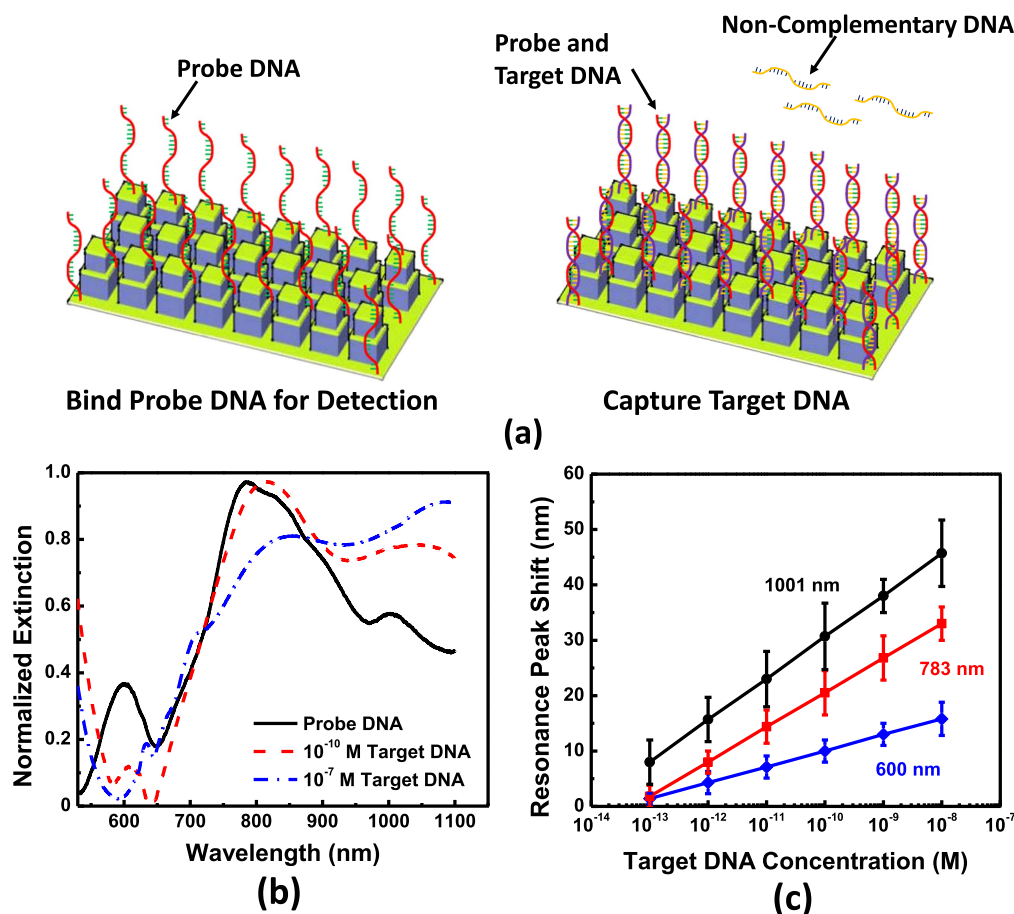


**Figure 7.** (a) Schematic for DNA hybridization detection. (b) Normalized extinction spectra of 3D multilayered plasmonic nanostructures with 56% offset and with probe and complementary target DNA of 10<sup>-10</sup> and 10<sup>-7</sup> M. (c) Resonance peak shift as function of complementary target DNA concentration.

10<sup>-14</sup>–10<sup>-7</sup> M. A large peak shift could be achieved because of the higher sensitivity and larger plasmonic sensor area of the 3D plasmonic nanostructures.

#### 4. Conclusions

3D multilayered plasmonic nanostructures with Au nanosquares on the top, Au asymmetrical nanostructures in the middle, and Au asymmetrical nanoholes at the bottom were fabricated using RNIL. The 3D multilayered plasmonic nanostructures showed higher EM field intensity and larger plasmon sensing area than 2D and quasi-3D plasmonic nanostructures. Thus, the 3D structures are promising as high sensitivity LSPR biosensors. The sensitivity and resonance peak wavelength of the 3D multilayered plasmonic biosensor were tunable by changing the offset between the top and bottom SU-8 nanopillars from 31% to 56%, and the highest sensitivities of 382 and 442 nm/RIU were obtained for resonance peaks at 581 and 805 nm, respectively. Resonance peak shifts of 36 and 52 nm for live A549 cells at  $5 \times 10^5$  cell ml<sup>-1</sup> occurred in the visible and near-infrared region and the detection range was  $5 \times 10^3$ – $5 \times 10^5$  cell ml<sup>-1</sup>. The 3D multilayered plasmonic biosensor also had the advantages of

detecting DNA hybridization at low concentration because of their larger plasmonic sensing area and enhanced EM field intensity from the hybrid plasmonic coupling of the Au layers on the top, middle, and bottom. The detection range for DNA hybridization was 10<sup>-14</sup>–10<sup>-7</sup> M complementary target DNA, and large peak shift of 82 nm was observed for capturing 10<sup>-7</sup> M complementary target DNA.

#### Acknowledgments

This work was supported by the Center for Biosystems, Neuroscience, and Nanotechnology (CBNN) of City University of Hong Kong (9360148, 9380062), the University Grants Council of Hong Kong (GRF Projects: 11210814, 11247716, and 11218017) and CRF project: C1013-15. We gratefully acknowledge all the members of CBNN and university cleanroom facilities for their help.

#### Conflict of interests

There are no conflicts to declare.



## ORCID iDs

Shuyan Zhu  <https://orcid.org/0000-0003-1393-9271>  
 Stella W Pang  <https://orcid.org/0000-0002-4330-0877>

## References

- [1] Roberts G C, Morris P G, Moss M A, Maltby S L, Palmer C A, Nash C E, Smart E, Holliday D L and Speirs V 2016 An evaluation of matrix-containing and humanised matrix-free 3-dimensional cell culture systems for studying breast cancer *PloS One* **11** e0157004
- [2] Pettitt J, Higgs E S, Adams R D, Jahrling P B and Hensley L E 2016 Use of existing diagnostic reverse-transcription polymerase chain reaction assays for detection of ebola virus RNA in semen *J. Infectious Dis.* **213** 1237
- [3] Garcia-Fonseca S, Ballesteros-Gomez A and Rubio S 2016 Restricted access supramolecular solvents for sample treatment in enzyme-linked immuno-sorbent assay of mycotoxins in food *Anal. Chim. Acta* **935** 129
- [4] Bedford E E, Boujday S, Pradier C M and Gu F X 2018 Spiky gold shells on magnetic particles for DNA biosensors *Talanta* **182** 259
- [5] Acimovic S S, Ortega M A, Sanz V, Berthelot J, Garcia-Cordero J L, Renger J, Maerkl S J, Kreuzer M P and Quidant R 2014 LSPR chip for parallel, rapid, and sensitive detection of cancer markers in serum *Nano Lett.* **14** 2636
- [6] Pires N M, Dong T, Hanke U and Hoivik N 2014 Recent developments in optical detection technologies in lab-on-a-chip devices for biosensing applications *Sensors* **14** 15458
- [7] García M, García-Carmona L and Escarpa A 2014 Microfluidic system for enzymeless electrochemical determination of inulin using catalytically active metal nanowires *Microchimica Acta* **182** 745
- [8] Chen J, Zheng Y, Tan Q, Shojaei-Baghini E, Zhang Y L, Li J, Prasad P, You L, Wu X Y and Sun Y 2011 Classification of cell types using a microfluidic device for mechanical and electrical measurement on single cells *Lab Chip* **11** 3174
- [9] Yanik A A, Huang M, Kamohara O, Artar A, Geisbert T W, Connor J H and Altug H 2010 An optofluidic nanoplasmonic biosensor for direct detection of live viruses from biological media *Nano Lett.* **10** 4962
- [10] Stockman M I 2015 Nanoplasmonic sensing and detection *Science* **348** 287
- [11] Wang X, Li Y, Wang H, Fu Q, Peng J, Wang Y, Du J, Zhou Y and Zhan L 2010 Gold nanorod-based localized surface plasmon resonance biosensor for sensitive detection of hepatitis B virus in buffer, blood serum and plasma *Biosen. Bioelectron.* **26** 404
- [12] Liu F, Wong M M, Chiu S K, Lin H, Ho J C and Pang S W 2014 Effects of nanoparticle size and cell type on high sensitivity cell detection using a localized surface plasmon resonance biosensor *Biosen. Bioelectron.* **55** 141
- [13] Howes P D, Chandrawati R and Stevens M M 2014 Colloidal nanoparticles as advanced biological sensors *Science* **346** 1247390
- [14] Messersmith R E, Nusz G J and Reed S M 2013 Using the localized surface plasmon resonance of gold nanoparticles to monitor lipid membrane assembly and protein binding *J. Phys. Chem. C* **117** 26725
- [15] Morales-Narváez E, Golmohammadi H, Naghdi T, Yousefi H, Kostiv U, Horák D, Pourreza N and Merkoçi A 2015 Nanopaper as an optical sensing platform *ACS Nano* **9** 7296
- [16] Anker J N, Hall W P, Lyandres O, Shah N C, Zhao J and Van Duyne R P 2008 Biosensing with plasmonic nanosensors *Nat. Mater.* **7** 442
- [17] Park J, Choi Y, Lee M, Jeon H and Kim S 2014 Novel and simple route to fabricate fully biocompatible plasmonic mushroom arrays adhered on silk biopolymer *Nanoscale* **7** 426
- [18] Zhu S, Li H, Yang M and Pang S W 2016 High sensitivity plasmonic biosensor based on nanoimprinted quasi 3D nanosquares for cell detection *Nanotechnology* **27** 295101
- [19] Li P et al 2016 Evaporative self-assembly of gold nanorods into macroscopic 3D plasmonic superlattice arrays *Adv. Mater.* **28** 2511
- [20] Hackett L P, Ameen A, Li W, Dar F K, Goddard L L and Liu G L 2018 Spectrometer-free plasmonic biosensing with metal-insulator-metal nanocup arrays *ACS Sensors* **3** 290
- [21] Rapisarda A, Giambianco N and Marletta G 2017 Kinetic discrimination of DNA single-base mutations by localized surface plasmon resonance *J. Colloid Interface Sci.* **487** 141
- [22] Huang C, Ye J, Wang S, Stakenborg T and Lagae L 2012 Gold nanoring as a sensitive plasmonic biosensor for on-chip DNA detection *Appl. Phys. Lett.* **100** 173114
- [23] Soares L, Csaki A, Jatschka J, Fritzsche W, Flores O, Franco R and Pereira E 2014 Localized surface plasmon resonance (LSPR) biosensing using gold nanotriangles: detection of DNA hybridization events at room temperature *Analyst* **139** 4964
- [24] Spadavecchia J, Barras A, Lyskawa J, Woisel P, Laure W, Pradier C M, Boukherroub R and Szunerits S 2013 Approach for plasmonic based DNA sensing: amplification of the wavelength shift and simultaneous detection of the plasmon modes of gold nanostructures *Anal. Chem.* **85** 3288
- [25] Yang X, Yu Y and Gao Z 2014 A highly sensitive plasmonic DNA assay based on triangular silver nanoprism etching *Acs Nano* **8** 4902
- [26] Singh Sekhon J and Verma S S 2011 Refractive index sensitivity analysis of Ag, Au, and Cu nanoparticles *Plasmonics* **6** 311
- [27] Rhee S W, Taylor A M, Tu C H, Cribbs D H, Cotman C W and Jeon N L 2005 Patterned cell culture inside microfluidic devices *Lab Chip* **5** 102
- [28] Yoon H J, Kozminsky M and Negrath S 2014 Emerging role of nanomaterials in circulating tumor cell isolation and analysis *ACS Nano* **8** 1995
- [29] Grönbeck H, Curioni A and Andreoni W 2000 Thiols and disulfides on the Au (111) surface: the headgroup-gold interaction *J. Am. Chem. Soc.* **122** 3839
- [30] Ye J, Hutchison J A, Uji-I H, Hofkens J, Lagae L, Maes G, Borghs G and Van Dorpe P 2012 Excitation wavelength dependent surface enhanced Raman scattering of 4-aminothiophenol on gold nanorings *Nanoscale* **4** 1606
- [31] Yang B and Pang S W 2006 Multiple level nanochannels fabricated using reversal UV nanoimprint *J. Vac. Sci. Technol. B* **24** 2984
- [32] Lahiri B, Khokhar A Z, Richard M, McMeekin S G and Johnson N P 2009 Asymmetric split ring resonators for optical sensing of organic materials *Opt. Express* **17** 1107
- [33] Stewart M E, Mack N H, Malyarchuk V, Soares J A, Lee T W, Gray S K, Nuzzo R G and Rogers J A 2006 Quantitative multispectral biosensing and 1D imaging using quasi-3D plasmonic crystals *Proc. Natl Acad. Sci. USA* **103** 17143
- [34] Zhao X, Wong M M, Chiu S K and Pang S W 2015 Effects of three-layered nanodisk size on cell detection sensitivity of plasmon resonance biosensors *Biosen. Bioelectron.* **74** 799
- [35] Rippa M, Castagna R, Tkachenko V, Zhou J and Petti L 2017 Engineered nanopatterned substrates for high-sensitive localized surface plasmon resonance: an assay on biomacromolecules *J. Mater. Chem. B* **5** 5473

- [36] Liu P, Chin L, Ser W, Chen H, Hsieh C-M, Lee C-H, Sung K-B, Ayi T, Yap P and Liedberg B 2016 Cell refractive index for cell biology and disease diagnosis: past, present and future *Lab Chip* **16** 634
- [37] Xu Y, Zhou S, Lam Y W and Pang S W 2017 Dynamics of natural killer cells cytotoxicity in microwell arrays with connecting channels *Front. Immunol.* **8** 998
- [38] Zhang W, Ji Y, Meng J, Wu X and Xu H 2012 Probing the behaviors of gold nanorods in metastatic breast cancer cells based on UV-vis-NIR absorption spectroscopy *PLoS One* **7** e31957
- [39] Ng S P, Qiu G, Ding N, Lu X and Wu C L 2016 Label-free detection of 3-nitro-L-tyrosine with nickel-doped graphene localized surface plasmon resonance biosensor *Biosens. Bioelectron.* **89** 468
- [40] Chen B, Mokume M, Liu C and Hayashi K 2014 Structure and localized surface plasmon tuning of sputtered Au nano-islands through thermal annealing *Vacuum* **110** 94
- [41] Geng Z, Kan Q, Yuan J and Chen H 2014 A route to low-cost nanoplasmonic biosensor integrated with optofluidic-portable platform *Sensors Actuators B* **195** 682
- [42] Focsan M, Craciun A M, Potara M, Leordean C, Vulpoi A, Maniu D and Astilean S 2017 Flexible and tunable 3D gold nanocups platform as plasmonic biosensor for specific dual LSPR-SERS immuno-detection *Sci. Rep.* **7** 14240
- [43] Mayer K M and Hafner J H 2011 Localized surface plasmon resonance sensors *Chem. Rev.* **111** 3828
- [44] Li A, Lim X, Guo L and Li S 2018 Quantitative investigation on the critical thickness of the dielectric shell for metallic nanoparticles determined by the plasmon decay length *Nanotechnology* **29** 165501
- [45] Omaghali N E, Tkachenko V, Andreone A and Abbate G 2013 Optical sensing using dark mode excitation in an asymmetric dimer metamaterial *Sensors* **14** 272
- [46] Thomsen V, Schatzlein D and Mercuro D 2003 Limits of detection in spectroscopy *Spectroscopy* **18** 112